Journal of Cleaner Production 368 (2022) 133089

Contents lists available at ScienceDirect

Journal of Cleaner Production

journal homepage: www.elsevier.com/locate/jclepro

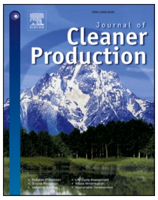

Copper oxide and manganese dioxide nanoparticles on corrugated glass-fiber supporters promote thermocatalytic oxidation of formaldehyde

Wen-Jun Qiang [a,1], Qing Huang [a,1], Jia-Hao Shen [a], Qin-Fei Ke [a], Jun-Ying Lü [b], Ya-Ping Guo [a,*]

[a] *The Education Ministry Key Lab of Resource Chemistry, Shanghai Key Laboratory of Rare Earth Functional Materials, Shanghai Normal University, Shanghai, 200234, PR China*
[b] *China Haisum Engineering CO., LTD, Shanghai, 200031, PR China*

ARTICLE INFO

Handling Editor: Prof. Jiri Jaromir Klemeš

Keywords:
Catalytic oxidation
Formaldehyde
Manganese dioxide
Copper oxide
Glass-fiber supporter

ABSTRACT

Low catalytic activity and difficult separation of manganese dioxide nanoparticles limit their application in the removal of volatile organic compounds (VOCs). Herein, copper oxide (CuO) and δ-manganese dioxide (MnO_2) catalysts were deposited uniformly on a glass-fiber supporter (GFS) by an in-situ precipitation method. The GFS with the hierarchical pores and great specific surface areas was employed as a catalytic supporter. The MnO_2 major catalysts and CuO cocatalysts synergistically promoted the formaldehyde thermocatalytic oxidation, and the removal efficiency arrived at nearly 100% even after cycle tests of 4 times. Thermodynamic calculation results demonstrated that the formaldehyde thermocatalytic oxidation over the CuO–MnO_2/GFS was performed via a Mars-van Krevelen mechanism. Namely, the formaldehyde molecules were oxidized by the copper oxide and δ-manganese dioxide, and then the as-produced cuprous oxide and manganese sesquioxide were re-oxidized into copper oxide and manganese dioxide by gas phase oxygen. Notably, copper oxide cocatalysts significantly improved the catalytic activity of the CuO–MnO_2/GFS because they not only directly participated in the formaldehyde oxidation but also promoted the oxidation reaction of manganese sesquioxide into manganese oxide. This work revealed the synergistic mechanism of MnO_2 major catalysts and CuO cocatalysts in promoting thermocatalytic oxidation of formaldehyde, and provided a promising thermocatalyst for the purification of industrial waste gas.

1. Introduction

Formaldehyde, one of ubiquitous volatile organic compounds (VOCs), is mainly originated from industrial waste gas (Tao et al., 2020). Long-term exposure to formaldehyde tends to cause neurological dementia (Kou et al., 2022), hematopoietic toxicity (Ge et al., 2020) and myeloid leukemia (Shallis et al., 2021). In order to prevent formaldehyde emissions from industrial production processes, various cleaner technologies such as adsorption (Zhou et al., 2021), photocatalysis (Talaiekhozani et al., 2021), thermo-electrochemistry (Yuan et al., 2017) and thermocatalysis (Lee et al., 2021) have been developed upon to now. Although adsorption technology is a simple and effective method to remove VOCs, it becomes invalid after adsorption saturation (Lu et al., 2021). Application of photocatalytic oxidation is limited because of low quantum efficiencies as well as extra photosources (Yang et al., 2021). Fortunately, thermocatalytic oxidation is an alternative approach for the complete degradation of VOCs into H_2O and CO_2 (Lee et al., 2021). Upon to now, thermocatalytic oxidation technology has been widely used for VOC emissions abatement because of its long-term reliability, high economic feasibility, and low levels of byproducts (Brummer et al., 2022). The thermocatalytic oxidation processes of VOCs are carried out in the fixed-bed reactors and fluidized-bed reactors (Guo et al., 2021). According to the chemical compositions and concentrations of VOCs, the temperatures on the reactor's inlet and outlet were commonly kept at 200–400 °C and 400–600 °C, respectively (Brummer et al., 2022). In order to reduce additional energy consumption, the development of highly efficient thermocatalysts with low operation temperatures is a promising strategy for the purification of industrial waste gas.

Thermocatalysts are mainly divided into noble metal catalysts (e.g., Pt, Au, Ag, Ru, Ir and Pd) and transition metal oxide catalysts (e.g., CuO, MnO_x, CeO_2, Co_3O_4, Fe_2O_3) (Wu et al., 2021). Noble metal catalysts

---

* Corresponding author.
E-mail address: ypguo@shnu.edu.cn (Y.-P. Guo).
[1] Wen-Jun Qiang and Qing Huang contributed equally to this work.

https://doi.org/10.1016/j.jclepro.2022.133089
Received 28 February 2022; Received in revised form 2 July 2022; Accepted 7 July 2022
Available online 11 July 2022

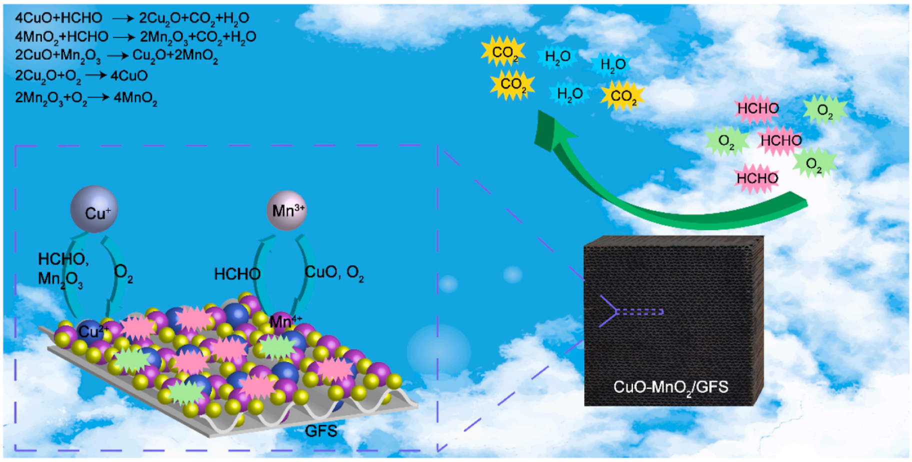

Fig. 1. Thermocatalytic model of CuO–MnO_2/GFS for formaldehyde oxidation.

possess excellent catalytic activity, but they show high cost and poor thermostability (Lee et al., 2021). Notably, manganese oxides are considered as a promising transition oxide catalyst for the degradation of VOCs because of their high catalytic activity, inexpensiveness and nontoxicity (Wu et al., 2021). The catalytic activity of manganese oxides (MnO_2) depends on their crystal phases and dopants (Wu et al., 2021). MnO_2 has different phase structures including α-, β-, γ-, δ-crystal types with the different tunnel sizes, active oxygen amounts and redox abilities (Zhang et al., 2015). Among four crystal forms, δ-MnO_2 exhibits the most amounts of active oxygen and lattice oxygen species on its crystal surfaces, leading to the highest thermocatalytic activity for HCHO oxidation (Zhang et al., 2015).

Besides the regulation of MnO_2 phases, another effective strategy is the combination of other metal oxides such as CeO_x (Chen et al., 2019), Co_3O_4 (Liu et al., 2022), NiO (Deng et al., 2018) and CuO (Li et al., 2017) with MnO_2 catalysts to improve the catalytic activity. For instance, the interfacial effect between cerium oxide and manganese dioxide plays a positive role in increasing catalytic activity (Chen et al., 2019). As the Ce/Mn molar ratio reaches 0.05, CeO_y/MnO_2 catalysts achieve higher acidity, more surficial oxygen vacancies and greater lattice oxygen mobility than pure MnO_2 catalysts (Chen et al., 2019). The Co_3O_4/MnO_2 interfaces (Liu et al., 2022) and NiO/MnO_2 interfaces (Deng et al., 2018) can also improve the vacancy contents, redox ability and lattice oxygen mobility, facilitating catalytic oxidation of VOCs. Copper metal, one of earth-abundant transition metals, is commonly recovered from electronic wastes. Sustainable recycling of copper metal contributes to alleviating depletion of resources and improving environmental sustainability (Fakayode and Nkambule, 2022). Fortunately, semiconducting copper oxides possess various oxidation states and oxygen adsorption properties, especially fit to detect and remove VOCs (Choi et al., 2019). The application of copper oxide catalysts may provide a new route for the sustainable recycling of copper metal (Fakayode and Nkambule, 2022). Recently, Li et al. (2017) prepared CuO/δ-MnO_2 hybrid catalysts by a self-propagated flaming technique. The highly dispersed CuO phase increases the lattice oxygen content as well as catalytic activity (Li et al., 2017). Density functional theory (DFT) simulations revealed that the Mn–O and Cu–O sites in the CuMn oxides facilitated toluene oxidation and toluene adsorption, respectively (Xiong et al., 2021). However, the synergistic effects between CuO and δ-MnO_2 on the enhanced thermocatalytic property still remained unknown.

Nanostructured MnO_2-based catalysts possessed excellent thermocatalytic activity on the oxidation of VOCs (Table S1), but they are difficultly separated from the reaction mixtures. Corrugated glass-fiber supporter (GFS) exhibits the cubic structured cartridge that is constructed by the accumulation of corrugated grid and flat grid along the same orientation (Zazhigalov et al., 2017). The specific geometrical structure of GFS makes it fit for a catalytic supporter in alkane oxidation (Zazhigalov et al., 2017), VOC degradation (Adebayo et al., 2020) and sulfur desulfurization (Larina et al., 2016). Herein, CuO and MnO_2 nanoparticles were deposited on the GFS surfaces for the thermocatalytic degradation of formaldehyde (Fig. 1). The MnO_2 major catalysts and CuO cocatalysts on the GFS synergistically promoted the complete degradation of formaldehyde into CO_2 and H_2O without undesirable byproducts, especially fit for the purification of high-temperature industrial waste gas. Moreover, thermodynamic calculation results proved that the formaldehyde thermocatalytic oxidation over the CuO–MnO_2/GFS was performed via the Mars-van Krevelen (MVK) mechanism. The main aims of this work were to fabricate CuO–MnO_2/GFS, to investigate its morphology, structure and catalytic property, and to reveal the synergistic effects between CuO and δ-MnO_2 for the formaldehyde thermal degradation.

2. Material and methods

2.1. Materials

GFS was purchased from Qingdao Huashijie Environment Technology Co., Ltd. Formaldehyde (HCOOH, A.R. grade) and copper nitrate trihydrate ($Cu(NO_3)_2 \cdot 3H_2O$, A.R. grade) were purchased from Shanghai Titan Scientific Co., Ltd. Potassium permanganate ($KMnO_4$, A.R. grade) was purchased from Shanghai Richjoint Chemical Reagents Co., Ltd. Anhydrous *n*-butanol [$CH_3(CH_2)_2CH_2OH$, A.R. grade] was purchased from Shanghai Hansi Chemical Industry Co., Ltd.

2.2. Synthesis of CuO–MnO_2/GFS

δ-MnO_2 nanoparticles were synthesized by using $KMnO_4$ and *n*-butanol as chemical reagents (Li et al., 2020). In this work, δ-MnO_2 and CuO nanoparticles were deposited on the GFS surfaces. In brief, $KMnO_4$ powders (3.790 g) were completely dissolved in 60 mL deionized water. The $Cu(NO_3)_2$ solutions with different concentrations of 0.1 mol/L, 0.2 mol/L, 0.3 mol/L and 0.4 mol/L were prepared by the dissolution of $Cu(NO_3)_2 \cdot 3H_2O$ powders in 60 mL deionized water, respectively. Anhydrous *n*-butanol (60 mL) was used as a reductant. 2.00 g GFS was immersed in the $KMnO_4$ solution for 60 s, anhydrous *n*-butanol for 300 s and $Cu(NO_3)_2$ solution for 60 s in turn. The cycled immersion was controlled at four times. The samples were dried at 60 °C for 12 h, and then calcined at 500 °C for 4 h. When the original $Cu(NO_3)_2$ concentrations were 0.1 mol/L, 0.2 mol/L, 0.3 mol/L and 0.4 mol/L, the corresponded thermocatalysts were abbreviated as 0.1CuO–MnO_2/GFS, 0.2CuO–MnO_2/GFS, 0.3CuO–MnO_2/GFS and 0.4CuO–MnO_2/GFS, respectively. Moreover, the MnO_2/GFS were prepared by the same

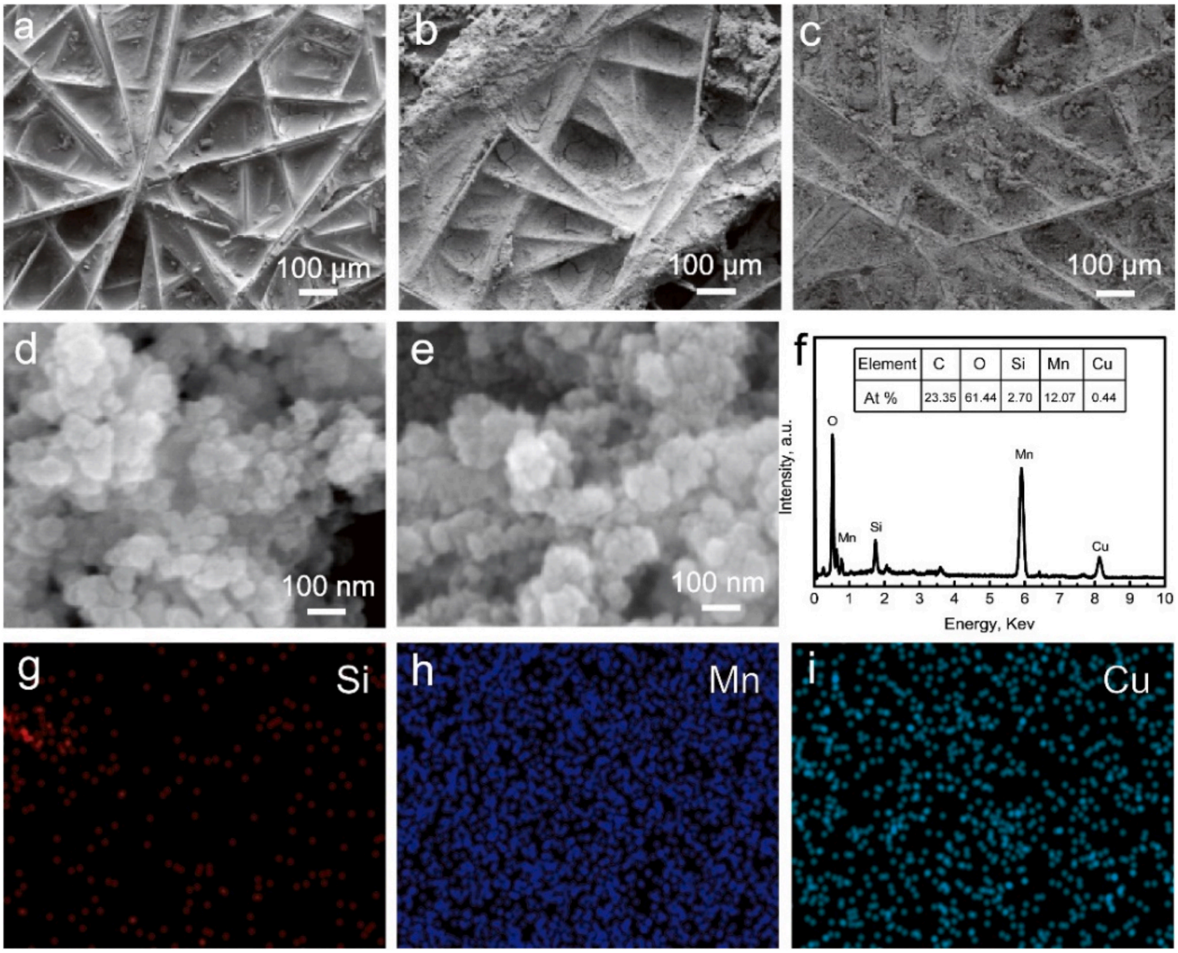

Fig. 2. Low-resolution SEM images: (a) GFS, (b) MnO_2/GFS and (c) 0.3CuO–MnO_2/GFS; high-resolution SEM images: (d) MnO_2/GFS and (e) 0.3CuO–MnO_2/GFS; (f) EDS spectrum of 0.3CuO–MnO_2/GFS; element distribution images of 0.3CuO–MnO_2/GFS: (g) Si, (h) Mn and (i) Cu.

method without immersing in $Cu(NO_3)_2$ solutions.

2.3. Characterization

The phases of GFS, MnO_2/GFS and CuO–MnO_2/GFS were analyzed by an X-ray diffraction (XRD, D/MAX-111 C, Japan) using Cu Kα radiation ($\lambda = 1.542$ Å) at 40 kV and 40 mA in the range of 10°~80° with a scan rate of $5^\circ\ min^{-1}$. The morphologies and elemental distributions of MnO_2/GFS and CuO–MnO_2/GFS were detected by field emission scanning electron microscopy (SEM, S4800, Hitachi) and energy dispersive spectrometer (EDS). The N_2 adsorption–desorption isotherms of GFS, MnO_2/GFS and CuO–MnO_2/GFS were measured by NOVA4000 (quantachrome) at 77 K. The Brunauer-Emmett-Teller (BET) surface areas of the above samples were calculated by a multipoint method using at least five adsorption points in the relative pressure (P/P_o) range of 0.05–0.30. The total pore volumes were evaluated at a relative pressure of 0.35. According to the desorption branches of the isotherms, the pore size distributions were determined by the Barrett-Joyner-Halanda (BJH) method. X-ray photoelectron spectroscopy (XPS) was carried out in Thermo Scientific K-Alpha at a pressure of 2×10^7 Torr. The binding energies of the Cu, Mn and O atoms were calibrated against a C1s of 284.6 eV. Hydrogen temperature-programmed reduction (H_2-TPR) measurements were performed on chemisorption analyzer (AutoChem II 2920). The H_2 consumption and the mass signal was detected by thermal conductivity (TCD) measurements.

2.4. Catalytic activity assay

100 mL HCHO solution (37–40 wt%) was added in a constant temperature bubbling device at 30 °C. High purity air (21% O_2, 79% N_2) was used as the power gas. After 0.50 g catalysts were filled into the tubular reactor, 460 ppm formaldehyde flew through the reactor. The catalytic reaction was carried out at 100–250 °C, and the gaseous hourly space velocity (GHSV) was kept at 30000–60000 mL $g^{-1}\cdot h^{-1}$. The concentrations of HCHO and CO_2 in the outlet gas were detected by a photoacoustic gas monitor (INNOVA 1412i, LumaSense Technologies, Denmark).

The HCHO removal efficiency (X_{HCHO}, %) was calculated by the following formula:

$$X_{HCHO} = \frac{C_{inlet} - C_{outlet}}{C_{inlet}} \times 100\ \% \tag{1}$$

where C_{inlet} and C_{outlet} were the concentration of toluene in inlet and outlet gas, respectively.

2.5. Thermodynamic calculation

Gibbs free energy change (ΔG) was a key thermodynamic parameter to evaluate the chemical reaction equilibrium. The ΔG values of the HCHO thermocatalytic oxidation reactions over CuO–MnO_2/GFS were calculated by the following equations (Panah, 2021):

$$\Delta G = \Delta_r H - T\Delta_r S \tag{2}$$

$$\Delta_r H = \sum v_i(\Delta H^{\theta}_{f,\,i}(T_{ref}) + \int_{T_{ref}}^{T} c_{p,i}(T)\mathrm{d}T \tag{3}$$

$$\Delta_r S = \sum v_i(\Delta S^{\theta}_{f,\,i}(T_{ref}) + \int_{T_{ref}}^{T} \frac{c_{p,i}(T)}{T}\mathrm{d}T \tag{4}$$

where Δ_rH, $\Delta_r S$, v_i, $c_{p,i}(T)$, $\Delta H^{\theta}_{f,\,i}(T_{ref})$, $\Delta S^{\theta}_{f,\,i}(T_{ref})$ were the molar enthalpy of reactions, molar entropy of reactions, stoichiometric coefficient of species *i*, heat capacity at constant pressure, molar enthalpy of formation and molar entropy of formation at the reference temperature (T_ref = 298.15 K), respectively.

3. Results and discussion

3.1. Morphology and porous structure of CuO–MnO$_2$/GFS

For the thermocatalytic oxidation of formaldehyde, CuO–MnO$_2$/GFS was fabricated by an in-situ precipitation method (Fig. 2). As show in the SEM images (Fig. 2a), the regular fringes were detected in the GFS surfaces. After the GFS was treated by the KMnO$_4$ solution, anhydrous *n*-butanol and Cu(NO$_3$)$_2$ solution in turn, MnO$_2$ nanoprticles were created on the GFS surfaces (Eq. (5)).

$$3CH_3CH_2CH_2CH_2OH+4KMnO_4 \rightarrow 3CH_3CH_2CH_2COOK+4MnO_2\downarrow+KOH+4H_2O \tag{5}$$

At the same time, part of Cu(NO$_3$)$_2$ was adsorbed in the GFS. After calcination at 500 °C for 4 h, the Cu(NO$_3$)$_2$ in the GFS decomposed thermally into CuO, O$_2$ and NO$_2$ (Eq. (6)).

$$Cu(NO_3)_2 \rightarrow CuO + O_2\uparrow+NO_2\uparrow \tag{6}$$

As compared with the pure GFS, the MnO$_2$/GFS and CuO–MnO$_2$/GFS showed the less fringes on their surfaces (Fig. 2a–c). The high-resolution SEM images indicated that the GFS surfaces became rough after the deposition of CuO and MnO$_2$ particles. The CuO and MnO$_2$ nanoparticles with sizes of approximately 50 nm were uniformly dispersed on the GFS surfaces (Fig. 2e and S1). The EDS spectrum and element distribution images indicated that the CuO–MnO$_2$/GFS was mainly composed of Si, Mn, Cu and O (Fig. 2f–i). The Si, Mn and Cu elements were originated from SiO$_2$, MnO$_2$ and CuO, respectively.

The nitrogen adsorption/desorption isotherms of the GFS, MnO$_2$/GFS and CuO–MnO$_2$/GFS were presented in Fig. 3a. According to the classification by International Union of Pure and Applied Chemistry (IUPAC), all the curves were considered as type V isotherms (Wang et al., 2014). The specific surface areas of the GFS, MnO$_2$/GFS and CuO–MnO$_2$/GFS were 124, 119 and 91 m^2 g^{-1}, respectively (Table 1). The pore size distribution curves indicated that the pore sizes of the GFS, MnO$_2$/GFS and CuO–MnO$_2$/GFS located at approximately 9.0 nm (Fig. 3b). These mesopores showed disordered characteristic, as confirmed by no limiting adsorption at P/P$_0$ = 0.9–1.0 (Wen et al., 2017). Moreover, the pore volumes of the GFS, MnO$_2$/GFS and CuO–MnO$_2$/GFS were 0.287, 0.285 and 0.248 cm^3 g^{-1}, respectively (Table 1). The specific surface areas and pore volumes of the GFS were slightly greater than those of the MnO$_2$/GFS and CuO–MnO$_2$/GFS (Table 1). The main reason could be attributed to the possibility that part of the pores within the GFS were blocked up by the CuO and MnO$_2$ nanoparticles (Yi et al., 2018).

3.2. Phases and valence states of CuO–MnO$_2$/GFS

The phases of GFS, MnO$_2$/GFS and CuO–MnO$_2$/GFS were characterized by the XRD patterns (Fig. 4). One broad peak at around 24° was detected in the XRD pattern of GFS, suggesting that the SiO$_2$ in the catalytic supporters exhibited an amorphous structure. For both the MnO$_2$/GFS and CuO–MnO$_2$/GFS, the diffraction peaks at 12.5°, 25.2°

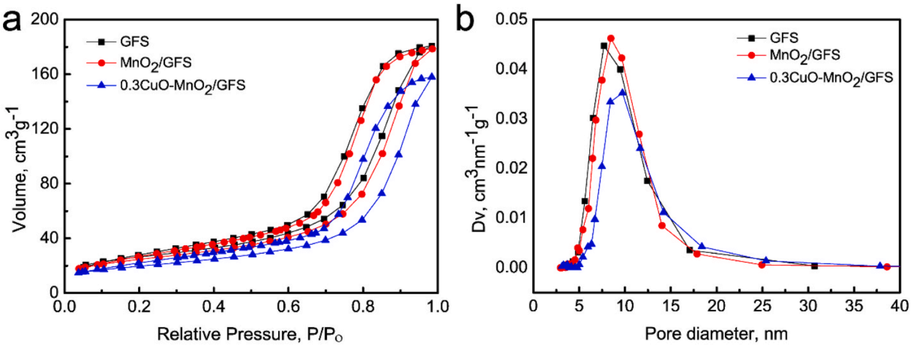

Fig. 3. (a) Nitrogen adsorption/desorption isotherms and (b) pore size distribution curves for GFS, MnO$_2$/GFS and 0.3CuO–MnO$_2$/GFS.

Table 1
The BET data, surface element compositions and H$_2$-TPR data of GFS, MnO$_2$/GFS and 0.3CuO–MnO$_2$/GFS.

Catalyst	Surface area, m^2•g^{-1}	Pore volume, cm^3•g^{-1}	Mn^{4+}/Mn^{3+} molar ratio	O$_{latt}$/O$_{ads}$ molar ratio	Cu^{2+}/Cu^{+} molar ratio	H$_2$ consumption, mmol•g^{-1}
GFS	124	0.287	/	/	/	0.143
MnO$_2$/GFS	119	0.285	0.40	0.37	/	1.356
0.3CuO–MnO$_2$/GFS	91	0.248	1.58	2.89	0.56	9.452

The symbol "/" indicated that the data did not exist.

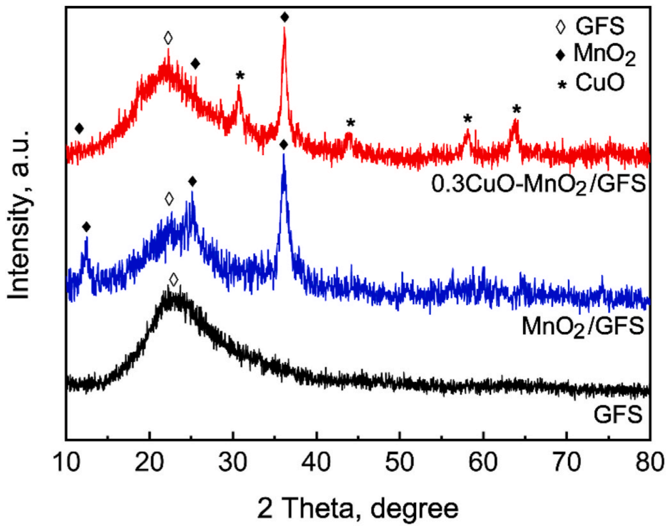

Fig. 4. XRD patterns of GFS, MnO_2/GFS and 0.3CuO–MnO_2/GFS.

and 37.1° corresponded to the (001), (002) and (−111) planes of δ-MnO_2 crystals, respectively (JCPDS 80–1098). In the XRD pattern of CuO–MnO_2/GFS, the peaks at 30.8°, 44.1°, 57.9° and 63.8° corresponded to the (110), (112), (202) and (113) planes of CuO crystals (JCPDS 05–0661). Both the CuO and MnO_2 in the catalysts showed the weak diffraction strength, suggesting their low crystallinity.

The element valence states of 0.3CuO–MnO_2/GFS were analyzed by XPS spectra (Fig. 5). The wide-scan XPS spectrum indicated that the CuO–MnO_2/GFS were composed of Si, Cu, Mn and O elements, which were in good agreement with the EDS result (Fig. 2f). According to the peak areas in Fig. 5a, the molar ratio of Cu:Mn in the 0.3CuO–MnO_2/GFS was calculated as 0.46:1. The Cu oxidation states in the CuO–MnO_2/GFS were examined by the curve-fitting XPS spectrum of Cu 2p (Fig. 5b). The characterized peaks due to Cu $2p_{3/2}$ and Cu $2p_{1/2}$ as well as satellite peaks indicated the coexistence of Cu^+ and Cu^{2+} ions (Bayat and Sheibani, 2022). The peaks at 933.9 and 954.0 eV corresponded to the Cu^{2+} state in CuO nanoparticles (Bayat and Sheibani, 2022). The satellite peaks at 941.6, 943.9 and 962.5 eV further confirmed the presence of the CuO in CuO–MnO_2/GFS (Fig. 5b). Besides the Cu^{2+} state, the characteristic peaks of Cu^+ state was also detected at 931.2, 932.6 and 951.3 eV (Fig. 5b) (Bayat and Sheibani, 2022). The binding energy of 931.2 eV were ascribed to Cu^+ with oxygen-vacancy (Cu^+-V_o), while that of 932.6 eV was ascribed to Cu^+ with oxygen-lattice (Cu^+O) (Choi and Jang, 2017). The Mn oxidation states in the CuO–MnO_2/GFS could be determined by the curve-fitting XPS spectrum of Mn 2p, too (Fig. 5c). The peaks at around 642.2 and 653.4 eV corresponded to Mn $2p_{3/2}$ and Mn $2p_{1/2}$, respectively (Mahamallik et al., 2015). The characterized Mn $2p_{3/2}$ peak could be deconvoluted into three peaks at 641.2, 642.6 and 644.0 eV, which corresponded to Mn^{3+}, Mn^{4+} and satellite, respectively (Mahamallik et al., 2015). The XPS spectra of Cu 2p and Mn 2p suggested that the Cu^{2+}/Cu^+ and Mn^{3+}/Mn^{4+} coexisted in the CuO–MnO_2/GFS. According to the characterized peak areas, the molar ratios of Cu^{2+}/Cu^+ and Mn^{4+}/Mn^{3+} in the catalysts were calculated as 0.56 and 1.58, respectively (Table 1). The XRD pattern indicated that only CuO and δ-MnO_2 phases without Cu_2O and Mn_2O_3 were detected in the CuO–MnO_2/GFS (Fig. 4). The reason could be attributed to the following possibilities: (i) both the Cu_2O and Mn_2O_3 in the CuO–MnO_2/GFS showed an amorphous structure; and (ii) parts of Cu^{2+} and Mn^{4+} ions in the CuO and δ-MnO_2 nanoparticles were respectively replaced by Cu^+ and Mn^{3+} ions, leading to the increase of oxygen-vacancy density. The thermal decomposition of $Cu(NO_3)_2$ to CuO, O_2 and NO_2 was a thermodynamically favored reaction (Eq. (6)). Notably, the as-formed CuO could be reduced into Cu_2O by Mn_2O_3 according to the following equation:

$$Mn_2O_3 + 2CuO \rightarrow MnO_2 + Cu_2O \quad (7)$$

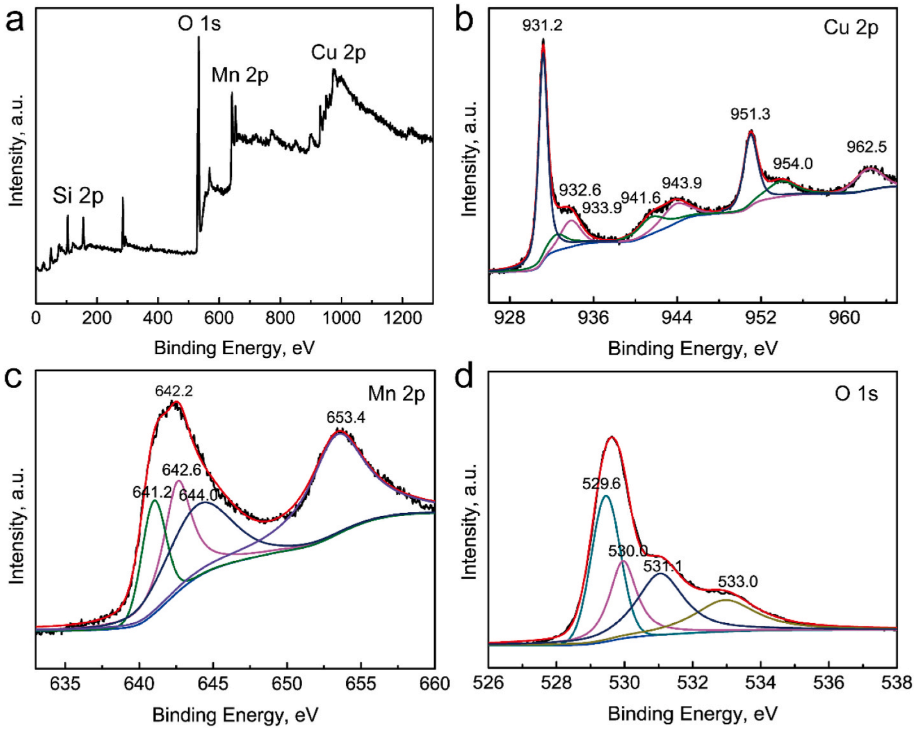

Fig. 5. The XPS spectra of 0.3CuO–MnO_2/GFS: (a) wide-scan spectrum; and curve-fitting analyses of (b) Cu 2p, (c) Mn 2p and (d) O 1s.

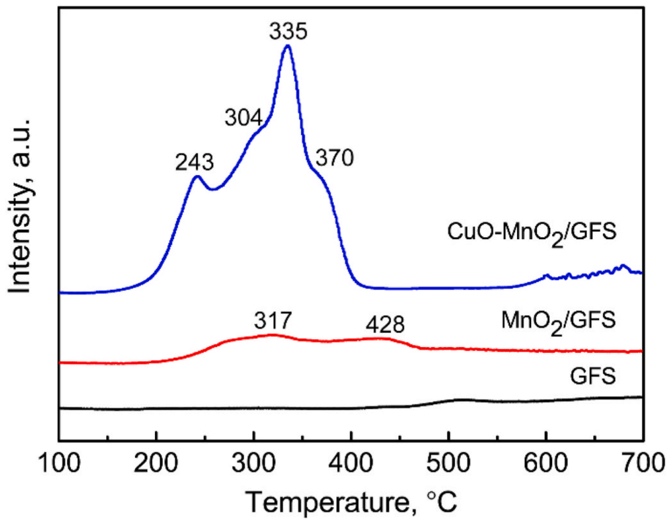

Fig. 6. (a) H_2-TPR profiles of GFS, MnO_2/GFS and 0.3CuO–MnO_2/GFS.

In order to prove the above reaction, the MnO_2/GFS was characterized by XPS spectra (Fig. S2). According to the curve-fitting XPS spectrum of Mn 2p, the molar ratio of Mn^{4+}/Mn^{3+} in the MnO_2/GFS was calculated as only 0.40, which was remarkably less than that of 1.58 in the CuO–MnO_2/GFS. The less Mn^{3+} ions in the CuO–MnO_2/GFS than those in the MnO_2/GFS further confirm the part consumption of Mn_2O_3 according to the above oxidation-reduction reaction (Eq. (7)).

The O 1s XPS spectrum of the CuO–MnO_2/GFS was shown in Fig. 5d, and quantitative results were listed in Table 1. Two peaks at 529.6 and 530.0 eV were attributed to the lattice oxygen (O_{latt}), while the peak at 531.1 eV corresponded to the adsorbed oxygen (O_{ads}) including O^{2-}, O_2^{2-} or O^- species (Liu et al., 2013). In addition, the peak due to adsorbed water on the CuO–MnO_2/GFS surfaces located at 533.0 eV. The O_{latt}/O_{ads} molar ratios in the CuO–MnO_2/GFS and MnO_2/GFS were 2.89 and 0.37, respectively (Table 1), suggesting that the modification of CuO in catalysts remarkably increased the O_{latt} amounts. The high O_{latt}/O_{ads} molar ratio could facilitate the catalytic degradation of VOCs such as benzene, ethylbenzene, toluene, and o-xylene (Liu et al., 2019).

3.3. Reducibility of CuO–MnO_2/GFS

The reducibility of CuO–MnO_2/GFS was evaluated by H_2-TPR analysis using GFS, MnO_2/GFS as control groups. Because GFS was mainly composed of SiO_2, it exhibited no reduction activity with H_2 at 100–700 °C (Fig. 6). The total H_2 consumption of 0.143 mmol g^{-1} was ascribed to the adsorbed oxygen on the GFS surfaces (Table 1). The H_2-TPR profile of MnO_2/GFS indicated two remarkable peaks centered at approximately 317 °C and 428 °C (Fig. 6). The first peak at around 200–360 °C was attributed to the reduction of MnO_2 to Mn_2O_3, while the second peak at around 360–480 °C was ascribed to the reduction of Mn_2O_3 to Mn_3O_4 (Le et al., 2021). Interestingly, the CuO dopants in the catalysts remarkably decreased the reduction temperatures of Mn species from 317 °C to 428 °C–304 °C and 370 °C, respectively (Fig. 6). The CuO–MnO_2/GFS showed the lower reduction temperatures than the MnO_2/GFS, demonstrating its more mobile oxygen species (Zhang et al., 2015). In addition, two new peaks due to the reduction of Cu species were detected in the H_2-TPR profile of 0.3CuO–MnO_2/GFS (Fig. 6). The peaks centered at 243 °C and 335 °C were ascribed to the reduction of CuO to Cu_2O and the reduction of Cu_2O to Cu^0, respectively (Deng et al., 2021). The total H_2 consumption amounts for MnO_2/GFS and 0.3CuO–MnO_2/GFS were 1.356 and 9.452 mmol g^{-1}, respectively (Table 1). Among three samples, 0.3CuO–MnO_2/GFS showed the greatest H_2 consumption due to the reduction of the adsorbed oxygen, Mn species and Cu species.

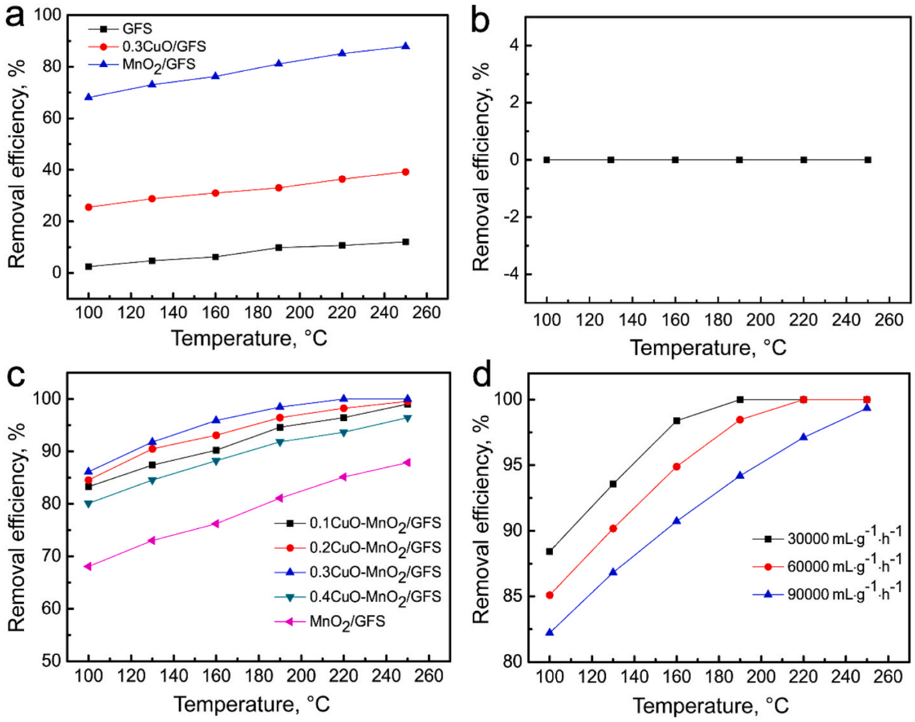

Fig. 7. (a) HCHO removal efficiencies as function of reaction temperatures over different catalysts (GHSV = 60000 mL g^{-1} h^{-1}); (b) HCHO removal efficiencies as function of reaction temperatures over 0.3CuO–MnO_2/GFS in N_2 atmosphere (GHSV = 60000 mL g^{-1} h^{-1}); (c) Effects of CuO doping amounts on HCHO removal efficiencies (GHSV = 60000 mL g^{-1} h^{-1}); (d) HCHO removal efficiencies over 0.3CuO–MnO_2/GFS under different GHSV.

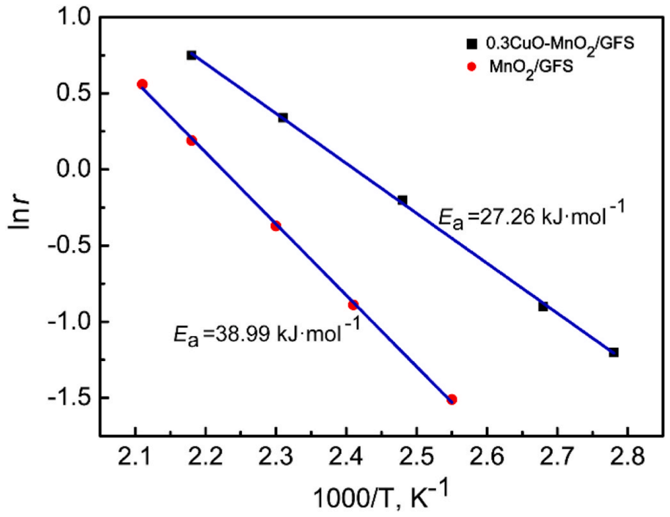

Fig. 8. Arrhenius plots over MnO_2/GFS and 0.3CuO–MnO_2/GFS for HCHO oxidation at GHSV = 60000 mL g^{-1} h^{-1}.

3.4. Thermocatalytic activities of CuO–MnO_2/GFS for formaldehyde oxidation

Thermocatalytic oxidation of VOCs over metal oxide catalysts is performed according to the MVK mechanism (Li et al., 2022). VOCs are oxidized by the surface lattice oxygen of metal oxide catalysts into H_2O and CO_2, leaving oxygen vacancies. The depleted lattice oxygen was replenished by gas phase oxygen, thereby regenerating active oxygen (Li et al., 2022). Upon to now, various thermocatalysts have been developed for catalytic oxidation of HCHO (Table S1). At high temperatures, the manganese oxide-based catalysts could effectively promote the thermal decomposition of formaldehyde into CO_2 and H_2O (Wu et al., 2021). However, these nano-catalysts were difficultly separated from industrial waste gas (Zhang et al., 2015). To overcome this disadvantage, the GFS served as the catalytic supporter of CuO and MnO_2 catalysts. The thermocatalytic performances of CuO–MnO_2/GFS with different copper oxide contents were evaluated in the temperature range of 100–250 °C (Fig. 7). In the presence of oxygen gas, formaldehyde could be oxidized into CO_2 and H_2O according to the following equation:

$$HCHO + O_2 \rightarrow CO_2 + H_2O \tag{8}$$

The Gibbs free energy change (ΔG) for the above chemical reaction equation was −620.38 kJ mol^{-1} at 250 °C (Table S2), suggesting that the formaldehyde oxidation was a thermodynamically favored reaction. Under the absence of oxygen gas, the formaldehyde oxidation reaction did not occur (Fig. 7b). The GFS that acted as a catalytic supporter showed the low catalytic activity for the formaldehyde degradation (Fig. 7a). MnO_2 and CuO were used as major catalysts and cocatalysts, respectively. The MnO_2 and CuO nanoparticles deposited on the GFS surfaces, respectively. Both the MnO_2/GFS and CuO/GFS possessed thermocatalytic activity for the formaldehyde oxidation, and the former was better than the latter in the temperature range of 100–250 °C (Fig. 7a).

The synergistic effect of MnO_2 and CuO promoted the HCHO degradation. All the CuO–MnO_2/GFS with different CuO doping amounts had better catalytic activity than the MnO_2/GFS under GHSV of 60000 mL g^{-1}·h^{-1} (Fig. 7c). Moreover, the modification of CuO in the catalysts significantly decreased the T_{90} values (the temperature of 90% HCHO removal). In addition, the doping amounts of CuO in the composite catalysts played an important role in the formaldehyde oxidation, and the order was as followed: 0.3CuO–MnO_2/GFS >0.2CuO–MnO_2/GFS >0.1CuO–MnO_2/GFS >0.4CuO–MnO_2/GFS > MnO_2/GFS (Fig. 7c). The HCHO removal efficiencies over all the catalysts increased as function of reaction temperatures. When the reaction temperature was over 220 °C, HCHO could be completely degraded by 0.3CuO–MnO_2/GFS (Fig. 7c). In addition, the GHSV remarkably affected the catalytic performances of CuO–MnO_2/GFS (Fig. 7d). The HCHO removal efficiencies over 0.3CuO–MnO_2/GFS decreased with the increase of GHSV, which could be attributed to the shortened contact time between the thermocatalyst and formaldehyde. The temperatures at which HCHO was completely removed decreased from 220 °C to 190 °C with increasing the GHSV from 30000 mL g^{-1}·h^{-1} to 90000 mL g^{-1}·h^{-1} (Fig. 7d). The above results suggested that the 0.3CuO–MnO_2/GFS exhibited excellent catalytic activity. Even if GHSV was kept at 90000 mL g^{-1}·h^{-1}, the total removal efficiency of formaldehyde was more than 95% at 250 °C.

For the formaldehyde oxidation, the apparent activation energies (E_a) over MnO_2/GFS and 0.3CuO–MnO_2/GFS were evaluated by Arrhenius equation (Tu et al., 2020):

$$r = Ae^{-E_a/RT} \tag{9}$$

where r, T, and A were the rate constant (s^{-1}), reaction temperature (K) and Arrhenius constant. According to the Arrhenius plots of ln$r$ versus 1000/T (Fig. 8), the E_a values for the MnO_2/GFS and 0.3CuO–MnO_2/GFS were 38.99 and 27.26 kJ mol^{-1}. The 0.3CuO–MnO_2/GFS showed the lower E_a value than the MnO_2/GFS, indicating that the modification of CuO could increase the formaldehyde oxidation rates.

The stability of 0.3CuO–MnO_2/GFS was evaluated under the GHSV of 60000 mL g^{-1}·h^{-1} (Fig. 9). In the initial stage, the catalytic tests were carried out at 200 °C for 16 h and then at 250 °C for 5 h. When the

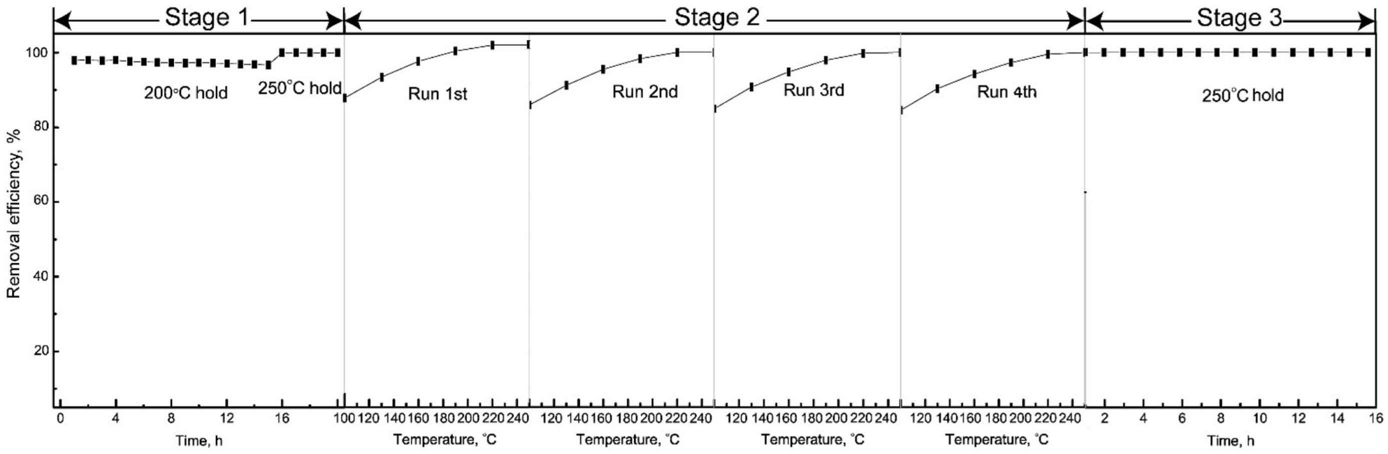

Fig. 9. Catalytic stability of 0.3CuO–MnO_2/GFS (GHSV = 60000 mL g^{-1} h^{-1}).

reaction temperature was kept at 200 °C, the HCHO removal efficiency was more than 97%. If the catalytic temperature increased upon to 250 °C, 100% HCHO was degraded. In the second stage, the test results of the following four cycles indicated that there was no significant difference among the HCHO removal curves as function of reaction temperatures over 0.3CuO–MnO_2/GFS. In the last stage, the catalytic reaction was performed at 250 °C for 16 h. The HCHO removal efficiency still maintained at 100% (Fig. 9). The above results demonstrated that 0.3CuO–MnO_2/GFS possessed high stability for the formaldehyde catalytic oxidation.

3.5. *Catalytic mechanism of CuO–MnO_2/GFS for HCHO oxidation*

The formaldehyde oxidation was a thermodynamically favored reaction in the presence of oxygen gas (Eq. (8)), but its reaction rate over the GFS without any catalyst was too slow to meet the demand of industrial application (Fig. 7a). Herein, the CuO–MnO_2/GFS was constructed by the deposition of CuO and δ-MnO_2 nanoparticles on the GFS surfaces (Figs. 2 and 4). The synergistic effects among the MnO_2 major catalysts, CuO cocatalysts and GFS contributed to the HCHO degradation into CO_2 and H_2O (Fig. 7). The HCHO catalytic oxidation processes over CuO–MnO_2/GFS could be divided into three steps: adsorption of formaldehyde, thermocatalytic oxidation reaction and desorption of degradation products (Tian et al., 2017). The GFS was especially fit for a catalytic carrier because of its hierarchically porous structures and great surface areas (Figs. 1–3). On the one hand, the corrugated macropores and mesopores in the GFS facilitated the transfer of organic pollutants and degradation products (Rong et al., 2020). On the other hand, the great surface area of the GFS contributed to capture HCHO and O_2, and thus facilitated the heterogeneous catalytic oxidation of HCHO over the CuO–MnO_2/GFS (Cui et al., 2019).

MnO_2 included α-, β-, γ-, δ-crystal phases among which δ-MnO_2 possessed the most excellent catalytic activity (Zhang et al., 2015). The δ-MnO_2 nanoparticles were the main active components of both the CuO–MnO_2/GFS and MnO_2/GFS (Figs. 2 and 4). Both Mn^{3+} and Mn^{4+} coexisted in the CuO–MnO_2/GFS and MnO_2/GFS, as confirmed by the XPS spectra (Fig. 5 and S1). Part of Mn^{3+} ions existed in the form of Mn_2O_3 with an amorphous structure, and the other existed in δ-MnO_2 by the replace of Mn^{4+} by Mn^{3+}. For both the CuO–MnO_2/GFS and MnO_2/GFS catalytic system, the MnO_2 and Mn_2O_3 played an essential role in the HCHO degradation. During the HCHO thermocatalytic process, the redox reactions of MnO_2/Mn_2O_3 were expressed by the following equations:

$$4MnO_2+HCHO\rightarrow 2Mn_2O_3+CO_2+H_2O \tag{10}$$

$$2Mn_2O_3+O_2\rightarrow 4MnO_2 \tag{11}$$

The ΔG values for Eqs. (10) and (11) were −516.75 and −13.26 kJ mol^{-1} respectively, suggesting the thermodynamically favored reactions (Table S2).

The MnO_2/GFS exhibited a good catalytic activity for the HCHO oxidation, but 12.1% HCHO were still remained even at 250 °C (Fig. 7a). Upon to now, various metal oxides such as NiO (Deng et al., 2018), TiO_2 (Mohamed and Awad, 2021), FeO_x (Dong et al., 2021), CeO_2 (Chen et al., 2019) and ZnO (Dai et al., 2020) were combined with MnO_2 for the catalytic degradation of VOCs. In this work, the CuO nanoparticles that served as a cocatalyst were deposited on the GFS surfaces (Figs. 2 and 4). Fortunately, the incorporation of copper oxide nanoparticles remarkably enhanced the catalytic activity of the CuO–MnO_2/GFS as compared with the MnO_2/GFS (Figs. 7 and 8). Firstly, both Cu^{2+} and Cu^{+} ions existed in the CuO–MnO_2/GFS, as proved by the XPS spectra (Fig. 5b). The redox reactions of CuO/Cu_2O took part in the formaldehyde oxidation, too:

$$4CuO + HCHO\rightarrow 2Cu_2O + CO_2+H_2O \tag{12}$$

$$2Cu_2O + O_2\rightarrow 4CuO \tag{13}$$

Thermodynamic calculation results revealed that Eqs. (12) and (13) with Δ$G < 0$ were thermodynamically favored reactions, too (Table S2). The catalytic tests further confirmed that the CuO/GFS facilitated the HCHO oxidation, although its catalytic activity was lower than the MnO_2/GFS (Fig. 7a). Secondly, the CuO in the composite catalysts promoted the oxidation reaction of Mn_2O_3 into MnO_2 (Eq. (7)), and then the as-formed MnO_2 participated in the HCHO oxidation (Eq. (10)). Thirdly, the lattice oxygen (O_{latt}) and adsorbed oxygen (O_{ads}) played an important role in the HCHO degradation (Qu et al., 2022). The HCHO oxidation processes over the CuO–MnO_2/GFS were controlled by MVK mechanism (Zhang et al., 2021). Namely, the formaldehyde molecules were oxidized by the surface lattice oxygen of CuO and MnO_2 (Eqs. (10) and (12)), and then as-produced Cu_2O and Mn_2O_3 were re-oxidized into CuO and MnO_2 by gas phase oxygen (Eqs. (11) and (13)). As shown in the H_2-TPR profiles, the H_2 total consumption for the CuO–MnO_2/GFS was significantly greater than that for the MnO_2/GFS (Fig. 6 and Table 1), suggesting that the incorporation of CuO dopants remarkably improved the O_{latt} and O_{ads} amounts. The abundant lattice oxygen in the CuO–MnO_2/GFS provided enough active sites for the HCHO catalytic oxidation (Huang et al., 2018). Finally, the CuO dopants increased the activation energy (E_a) of the CuO–MnO_2/GFS to 27.26 kJ mol^{-1}, which was remarkably lower than the MnO_2/GFS of 38.99 kJ mol^{-1}. The lower E_a value of the CuO–MnO_2/GFS than the MnO_2/GFS led to the greater HCHO degradation rate. Even at 190 °C, the HCHO could be completely oxidized by the CuO–MnO_2/GFS. For the 0.1CuO–MnO_2/GFS, 0.2CuO–MnO_2/GFS and 0.3CuO–MnO_2/GFS, the CuO cocatalysts played a positive role in the HCHO removal (Fig. 7c). However, the excessive CuO nanoparticles in the 0.4CuO–MnO_2/GFS tended to occupy the active sites of the δ-MnO_2, and thus decreased the catalytic activity in terms of formaldehyde oxidation (Cheng et al., 2021).

4. Conclusions

In summary, the CuO–MnO_2/GFS was prepared for the thermocatalytic oxidation of formaldehyde. The CuO and δ-MnO_2 nanoparticles with sizes of approximately 50 nm were uniformly distributed on the GFS surfaces. The GFS possessed the hierarchically porous structures and great specific surface areas, which supported the oxygen/formaldehyde transfer and the subsequent HCHO thermocatalytic oxidation. The synergistic effects between MnO_2 major catalysts and CuO cocatalysts made the CuO–MnO_2/GFS have better thermocatalytic activity than the MnO_2/GFS. Thermodynamic calculation results revealed that the CuO cocatalysts in the CuO–MnO_2/GFS not only directly took part in the formaldehyde oxidation but also facilitated the oxidation reaction of Mn_2O_3 into MnO_2. The CuO dopants increased the O_{latt} and O_{ads} amounts in the CuO–MnO_2/GFS, which contributed to the HCHO catalytic degradation. In addition, the CuO–MnO_2/GFS showed the lower apparent activation energy than the MnO_2/GFS, leading to the greater HCHO oxidation rates. The catalytic tests further demonstrated that the CuO–MnO_2/GFS could completely remove HCHO at 190 °C, and possessed good stability for the HCHO thermocatalytic oxidation. Therefore, the CuO–MnO_2/GFS with excellent catalytic activity may become a promising platform for the thermocatalytic oxidation of VOCs.

CRediT authorship contribution statement

Wen-Jun Qiang: Methodology, Investigation, Writing – original draft. **Qing Huang:** Investigation, Writing – review & editing. **Jia-Hao Shen:** Investigation, Writing – original draft. **Qin-Fei Ke:** Conceptualization, Supervision. **Jun-Ying Lü:** Methodology, Writing – review & editing. **Ya-Ping Guo:** Conceptualization, Supervision, Writing – review & editing, Funding acquisition.

Declaration of competing interest

The authors declare that they have no known competing financial interests or personal relationships that could have appeared to influence the work reported in this paper.

Data availability

Data will be made available on request.

Acknowledgements

This research was supported by Shanghai Science and Technology Committee (No. 18070502700) and Shanghai Engineering Research Center of Green Energy Chemical Engineering (No. 18DZ2254200).

Appendix A. Supplementary data

Supplementary data to this article can be found online at https://doi.org/10.1016/j.jclepro.2022.133089.

References

Adebayo, B.O., Newport, K., Yu, H., Rownaghi, A.A., Liang, X., Rezaei, F., 2020. Atomic layer deposited Ni/ZrO_2-SiO_2 for combined capture and oxidation of VOCs. ACS Appl. Mater. Interfaces 12, 39318–39334.

Bayat, F., Sheibani, S., 2022. Enhancement of photocatalytic activity of CuO-Cu_2O heterostructures through the controlled content of Cu_2O. Mater. Res. Bull. 145, 111561.

Brummer, V., Teng, S.Y., Jecha, D., Skryja, P., Vavrcikova, V., Stehlik, P., 2022. Contribution to cleaner production from the point of view of VOC emissions abatement: a review. J. Clean. Prod. 361, 132112.

Chen, J., Chen, X., Yan, D., Jiang, M., Xu, W., Yu, H., Jia, H., 2019. A facile strategy of enhancing interaction between cerium and manganese oxides for catalytic removal of gaseous organic contaminants. Appl. Catal. B Environ. 250, 396–407.

Cheng, W.K., Guo, C.X., Ke, Q.F., Guo, Y.P., 2021. Heavy metal ions in wastewater affect the photodegradation of phenol-4-sulfonic acid over biphasic TiO_2/activated carbon fiber composites. ChemistrySelect 6, 4336–4343.

Choi, D., Jang, D.J., 2017. Facile fabrication of CuO/Cu_2O composites with high catalytic performances. New J. Chem. 41, 2964.

Choi, Y.M., Cho, S.Y., Jang, D., Koh, H.J., Choi, J., Kim, C.H., Jung, H.T., 2019. Ultrasensitive detection of VOCs using a high-resolution CuO/Cu_2O/Ag nanopattern sensor. Adv. Funct. Mater. 29, 1808319.

Cui, F., Han, W., Si, Y., Chen, W., Zhang, M., Kim, H.Y., Ding, B., 2019. In situ synthesis of MnO_2@SiO_2–TiO_2 nanofibrous membranes for room temperature degradation of formaldehyde. Compos. Commun. 16, 61–66.

Dai, Z., Zhu, J., Yan, J., Su, J., Gao, Y., Zhang, X., Ke, Q., Parsons, G.N., 2020. An advanced dual-function MnO_2-fabric air filter combining catalytic oxidation of formaldehyde and high-efficiency fine particulate matter removal. Adv. Funct. Mater. 30, 2001488.

Deng, Y., Shi, X., Wei, L., Liu, H., Li, J., Ou, X., Dong, L., Li, B., 2021. Effect of intergrowth and coexistence CuO-CeO_2 catalyst by grinding method application in the catalytic reduction of NO_x by CO. J. Alloys Compd. 869, 159231.

Deng, Y., Tang, W., Li, W., Chen, Y., 2018. MnO_2-nanowire@NiO-nanosheet core-shell hybrid nanostructure derived interfacial Effect for promoting catalytic oxidation activity. Catal. Today 308, 58–63.

Dong, Y., Su, C., Liu, K., Wang, H., Zheng, Z., Zhao, W., Lu, S., 2021. The catalytic oxidation of formaldehyde by FeO_x-MnO_2-CeO_2 catalyst: effect of iron modification. Catalysts 11, 555.

Fakayode, O.J., Nkambule, T.T.I., 2022. Development of floating 3D-microfloral CuO-polysulfone beads for wastewater treatment. J. Water Proc. Eng. 46, 102530.

Ge, J., Yang, H., Lu, X., Wang, S., Zhao, Y., Huang, J., Xi, Z., Zhang, L., Li, R., 2020. Combined exposure to formaldehyde and PM2.5: hematopoietic toxicity and molecular mechanism in mice. Environ. Int. 144, 106050.

Guo, Y., Wen, M., Li, G., An, T., 2021. Recent advances in VOC elimination by catalytic oxidation technology onto various nanoparticles catalysts: a critical review. Appl. Catal. B Environ. 281, 119447.

Huang, N., Qu, Z., Dong, C., Qin, Y., Duan, X., 2018. Superior performance of α@β-MnO_2 for the toluene oxidation: active interface and oxygen vacancy. Appl. Catal., A 560, 195–205.

Kou, Y., Zhao, H., Cui, D., Han, H., Tong, Z., 2022. Formaldehyde toxicity in age-related neurological dementia. Ageing Res. Rev. 73, 101512.

Larina, T.V., Cherepanova, S.V., Rudina, N.A., Kolesov, B.A., Zagoruiko, A.N., 2016. Characterization of vanadia catalysts on structured micro-fibrous glass supports for selective oxidation of hydrogen sulfide. Catal. Sustain. Energy 2, 87–95.

Le, M.T., Singh, S., Nguyen-Quang, M., Ngo, A.B., Brückner, A., Armbruster, U., 2021. Insight into the properties of MnO_2-Co_3O_4-CeO_2 catalyst series for the selective catalytic reduction of NO_x by C_3H_6 and NH_3. Sci. Total Environ. 784, 147394.

Lee, Y.-J., Vikrant, K., Szulejko, J.E., Kim, K.-H., Dong, F., 2021. Thermocatalytic oxidation of a three-component mixture of volatile organic compounds by a titanium dioxide-supported platinum catalyst. J. Clean. Prod. 325, 129279.

Li, L., Luo, J., Liu, Y., Jing, F., Su, D., Chu, W., 2017. Self-propagated flaming synthesis of highly active layered CuO-δ-MnO_2 hybrid composites for catalytic total oxidation of toluene pollutant. ACS Appl. Mater. Interfaces 9, 21798–21808.

Li, R., Zhang, L., Zhu, S., Fu, S., Dong, X., Ida, S., Zhang, L., Guo, L., 2020. Layered δ-MnO_2 as an active catalyst for toluene catalytic combustion. Appl. Catal. Gen. 602, 117715.

Li, X., Niu, Y., Su, H., Qi, Y., 2022. Simple thermocatalytic oxidation degradation of VOCs. Catal. Lett. 152, 1801–1818.

Liu, L., Li, J., Zhang, H., Li, L., Zhou, P., Meng, X., Guo, M., Jia, J., Sun, T., 2019. In situ fabrication of highly active γ-MnO_2/$SmMnO_3$ catalyst for deep catalytic oxidation of gaseous benzene, ethylbenzene, toluene, and o-xylene. J. Hazard Mater. 362, 178–186.

Liu, W., Xiang, W., Guan, N., Cui, R., Cheng, H., Chen, X., Song, Z., Zhang, X., Zhang, Y., 2022. Enhanced catalytic performance for toluene purification over Co_3O_4/MnO_2 catalyst through the construction of different Co_3O_4-MnO_2 interface. Separ. Purif. Technol. 278, 119590.

Liu, Y., Dai, H., Deng, J., Du, Y., Li, X., Zhao, Z., Wang, Y., Gao, B., Yang, H., Guo, G., 2013. In situ poly(methyl methacrylate)-templating generation and excellent catalytic performance of MnO_x/3DOM $LaMnO_3$ for the combustion of toluene and methanol. Appl. Catal. B Environ. 140–141, 493–505.

Lu, S., Liu, Q., Han, R., Guo, M., Shi, J., Song, C., Ji, N., Lu, X., Ma, D., 2021. Potential applications of porous organic polymers as adsorbent for the adsorption of volatile organic compounds. J. Environ. Sci. 105, 184–203.

Mahamallik, P., Saha, S., Pal, A., 2015. Tetracycline degradation in aquatic environment by highly porous MnO_2 nanosheet assembly. Chem. Eng. J. 276, 155–165.

Mohamed, E.F., Awad, G., 2021. Hollow N-TiO_2/MnO_2 nanocomposite based yeast biomass for gaseous formaldehyde degradation under visible light. J. Ind. Eng. Chem. 98, 366–374.

Panah, H.S., 2021. Gibbs free energy change using Ru/Al_2O_3 catalyst – an application in supercritical water gasification process. Int. J. Hydrogen Energy 46, 27444–27458.

Qu, Y., Zheng, X., Ma, K., He, W., Wang, S., Zhang, P., 2022. Facile coating of MnO_2 nanoparticles onto polymer fibers via friction-heating adhesion for efficient formaldehyde removal. Chem. Eng. J. 430, 132954.

Rong, S., He, T., Zhang, P., 2020. Self-assembly of MnO_2 nanostructures into high purity three-dimensional framework for high efficiency formaldehyde mineralization. Appl. Catal. B Environ. 267, 118375.

Shallis, R.M., Weiss, J.J., Deziel, N.C., Gore, S.D., 2021. Challenging the concept of de novo acute myeloid leukemia: environmental and occupational leukemogens hiding in our midst. Blood Rev. 47, 100760.

Tao, Y., Li, R., Huang, A.B., Ma, Y.N., Ji, S.D., Jin, P., Luo, H.J., 2020. High catalytic activity for formaldehyde oxidation of an interconnected network structure composed of δ-MnO_2 nanosheets and γ-MnOOH nanowires. Adv. Manuf. 8, 429–439.

Talaiekhozani, A., Rezania, S., Kim, K.H., Sanaye, R., Amani, A.M., 2021. Recent advances in photocatalytic removal of organic and inorganic pollutants in air. J. Clean. Prod. 278, 123895.

Tian, M.J., Liao, F., Ke, Q.F., Guo, Y.J., Guo, Y.P., 2017. Synergetic effect of titanium dioxide ultralong nanofibers and activated carbon fibers on adsorption and photodegradation of toluene. Chem. Eng. J. 328, 962–976.

Tu, J., Sang, L., Cheng, H., Ai, N., Zhang, J., 2020. Continuous hydrogenolysis of N-diphenylmethyl groupsina micropacked-bed reactor. Org. Process Res. Dev. 24, 59–66.

Wang, M., Liu, H., Huang, Z.H., Kang, F., 2014. Activated carbon fibers loaded with MnO_2 for removing NO at room temperature. Chem. Eng. J. 256, 101–106.

Wen, X., Yang, F., Ke, Q.F., Xie, X.T., Guo, Y.P., 2017. Hollow mesoporous ZSM-5 zeolite/chitosan ellipsoids loaded with doxorubicin as pH-responsive drug delivery systems against osteosarcoma. J. Mater. Chem. B 5, 7866.

Wu, P., Jin, X., Qiu, Y., Ye, D., 2021. Recent progress of thermocatalytic and photo/thermocatalytic oxidation for VOCs purification over manganese-based oxide catalysts. Environ. Sci. Technol. 55, 4268–4286.

Xiong, S., Huang, N., Peng, Y., Chen, J., Li, J., 2021. Balance of activation and ring-breaking for toluene oxidation over CuO-MnO_x bimetallic oxides. J. Hazard Mater. 415, 125637.

Yang, T.Y., Liu, Y., Xia, G.D., Zhu, X.D., Zhao, Y., 2021. Degradation of formaldehyde and methylene blue using wood-templated biomimetic TiO_2. J. Clean. Prod. 329, 129726.

Yi, Y., Li, C., Zhao, L., Du, X., Gao, L., Chen, J., Zhai, Y., Zeng, G., 2018. The synthetic evaluation of CuO-MnO_x-modified pinecone biochar for simultaneous removal formaldehyde and elemental mercury from simulated flue gas. Environ. Sci. Pollut. Res. 25, 4761–4775.

Yuan, D.D., Tian, L., Gu, D., Shen, X.Y., Zhu, L.Y., Wu, H.J., Wang, B.H., 2017. Fast and efficient oxidation of formaldehyde in wastewater via the Solar Thermal Electrochemical Process tuned by thermo-electrochemistry. J. Clean. Prod. 156, 310–316.

Zazhigalov, S., Elyshev, A., Lopatin, S., Larina, T., Cherepanova, S., Mikenin, P., Pisarev, D., Baranov, D., Zagoruiko, A., 2017. Copper-chromite glass fiber catalyst and its performance in the test reaction of deep oxidation of toluene in air. Kinet. Mech. Cat. 120, 247–260.

Zhang, J., Li, Y., Wang, L., Zhang, C., He, H., 2015. Catalytic oxidation of formaldehyde over manganese oxides with different crystal structures. Catal. Sci. Technol. 5, 2305–2313.

Zhang, X., Yang, Y., Zhu, Q., Ma, M., Jiang, Z., Liao, X., He, C., 2021. Unraveling the effects of potassium incorporation routes and positions on toluene oxidation over α-MnO_2 nanorods: based on experimental and density functional theory (DFT) studies. J. Colloid Interface Sci. 598, 324–338.

Zhou, D., Li, Z., Sun, Y., Zhang, J., Wang, D., Shao, X., 2021. Adsorption of formaldehyde on the ZnO(101¯0) surface: a low-temperature STM study. J. Phys. Chem. C 125, 25859–25866.